JOURNAL OF SOLID STATE CHEMISTRY **121,** 379–387 (1996)
ARTICLE NO. 0051

Structural Studies of Tungsten–Titanium Oxide Thin Films

L. E. Depero,* S. Groppelli,* I. Natali-Sora,* L. Sangaletti,* G. Sberveglieri,* and E. Tondello†

**Dipartimento di Chimica e Fisica per i Materiali, Università di Brescia, Via Branze 38, 25123 Brescia; and †Dipartimento di Chimica Inorganica, Metallorganica e Analitica, Università di Padova, Via F. Marzolo, I-35131 Padova, Italy*

Received April 12, 1995; in revised form August 30, 1995; accepted October 19, 1995

Structural studies of tungsten–titanium oxide thin films grown on alumina substrates have been performed on samples prepared by reactive magnetron sputtering of a W/Ti alloy (90% W and 10% Ti). Structural changes undergone by samples heated at 773 and 1073 K have been studied by using X-ray diffraction and X-ray photoemission techniques. The results, which have been also discussed with the aid of a structural model, indicate that the original amorphous phase transforms by annealing into a crystalline phase of tungsten oxide with a degree of order depending on the annealing temperature. The relationship between titanium and the structure of the film is discussed in terms of disorder effects induced by the Ti ions in the WO_3 lattice. The ordering is ascribed to the segregation of Ti ions toward the surface upon annealing at 1073 K.

© 1996 Academic Press, Inc.

INTRODUCTION

Tungsten trioxide (WO_3) has important electrical and electrochromic properties (1) and amorphous or polycrystalline tungsten oxide films show remarkable catalytic activity in both oxidation and reduction reactions (2). The widespread interest in the potential applications of this material in water photolysis, in the coating of electric displays, and as a gas sensor has prompted many studies aiming at the production of WO_3-based devices (3, 4). In particular, WO_3-based sensors can detect low concentrations (10 ppm) of NO_x, H_2S, and NH_3 in the 473–773 K temperature range and, for this reason, they are good candidates as exhaust gas sensors for automobile engines and thermal power reactors.

Many phases have been detected in the WO_3 system, all related to the ReO_3 cubic structure (5). Since the formation of these phases can be related to the oxygen content, it is very likely that also the properties of these materials are related to the stoichiometry of the film. Indeed, it was found that the oxygen content plays a fundamental role in the photochromic effect of these materials (6). The phase formation and the microstructure depend on the type of film-growing conditions. Different preparation techniques have been reported (7–11) indicating the criticalness of these processes. For all these reasons, the study of the structural changes in the thin films of WO_3 is mandatory. Particular attention must also be paid to the influence of other transition metals that are often added to improve the film characteristics when used as a gas sensor.

Recently, with the aim of obtaining stable gas sensors, thin films of WO_3 were grown on alumina substrates by reactive sputtering and their structural and electrical properties were studied (12). The as-grown films showed orthorhombic WO_3 diffraction patterns and low crystallinity. In addition, after thermal treatments the films showed poor adhesive properties. To improve their adhesion to the substrate, Ti atoms were added to WO_3, using for the sputtering process a metallic target of a W/Ti alloy (90% of W and 10% of Ti).

As regards the interplay of Ti/W, it was already found that amorphous WO_3–TiO_2 thin films have a prolonged lifetime of electrochromism (3) and comparisons have been performed between thin films produced by sputtering and those obtained by the sol–gel technique (13). Moreover, the effects of W on the stability of the catalysts based on TiO_2 powders are known (14) and its influence on the surface acidity has been studied (15).

Notwithstanding the structural compatibility of W and Ti in the oxides and the diffusion of W in the TiO_2 structure, no mixed oxide containing only Ti and W was found in the Inorganic Crystal Structure Database (ICSD) (16) or the Power Diffraction File (PDF) database (17). However, in structures where, in addition to W, Ti and other cations are present, W and Ti share the same positions (16).

In what follows, the influence of Ti on structural changes, after annealing of these films (at 773 and 1073 K), will be discussed on the basis of X-ray diffraction and X-ray photoemission experiments. Annealing was performed to study the structural stability upon heat treatment in air at a usual temperature for sensor applications (773 K), as well as at a higher temperature (1073 K) to investigate, in

0022-4596/96 $18.00
Copyright © 1996 by Academic Press, Inc.
All rights of reproduction in any form reserved.

addition to structural transformations, the adhesion properties of the thin film to the alumina substrate.

EXPERIMENTAL

Thin films were deposited onto a 10 × 10 × 0.5 mm^3 polycrystalline alumina substrate (purity, 99.6%; grain size, 1.5–2.5 μm average diameter) by r.f. magnetron sputtering (ALCATEL SCM 450) from a target of a W/Ti alloy (90% W and 10% Ti). During the deposition, the substrate was held at 573 K in an argon/oxygen gas mixture ($P_{Ar} = P_{O_2} = 4 \times 10^{-1}$ Pa). The deposition rate was 0.36 nm/s and the thin-film thickness measured by a depth profilometer (TENCOR INSTR., Mod. ALPHA STEP) was 1.3 μm.

In order to assess the thermal stability of the films, two samples were annealed for 18 hours in air at 773 and 1073 K, respectively.

X-ray diffraction (XRD) measurements were performed on a Philips MPD 1880 powder diffractometer with a graphite monochromated Cu$K\alpha$ radiation in the Bragg–Brentano parafocusing geometry. The sample holder did not contribute to the diffraction patterns.

X-ray photoemission spectroscopy (XPS) spectra were recorded in a Perkin–Elmer PHI 5600*ci* spectrometer using monocromated Al$K\alpha$ radiation (1486.6 eV). The working pressure in the system was less than 1×10^{-8} Pa. To overcome sample charging, an e^- flood gun was used as a neutralizer. The spectrometer was calibrated by assuming the binding energy of the Au $4f_{7/2}$ line to be 83.9 eV with respect to the Fermi level. Survey scans were obtained in the range 0–1200 eV, while detailed scans were recorded for C 1*s*, Ti 2*p*, W 4*f*, and O 1s peaks. The atomic compositions were evaluated using sensitivity factors as provided by PHI V5.4A software. Sample sputtering was carried out by Ar^+ at 2.5 keV, 4×10^{-3} mA mm^{-2} beam current density with an argon partial pressure of 5×10^{-6} Pa.

Simulated XRD patterns were generated using the program Cerius^2, developed by Molecular Simulations Incorporated.

RESULTS AND DISCUSSION

The X-ray diffraction patterns of as-grown thin films are shown in Fig. 1, where a logarithmic scale for the signal intensity is used to emphasize the amorphous halo. In Fig. 2 the patterns detected after thermal treatments at 773 K (Fig. 2b) and 1073 K (Fig. 2c) are compared with the pattern obtained for a polycrystalline sample of orthorhombic WO_3 (Fig. 2d). The powder pattern of the crystalline phase of the sample annealed at 773 K matches that of the tetragonal phase of $WO_{2.9}$ (PDF card 18-1417 (17), Fig. 2a), with a small but significant shift of the peaks toward lower 2θ angles (see Table 1). Since it is hard to believe that such a phase, with tungsten in a reduced state, can exist after a thermal treatment, for explaining the observed profile a partial substitution of Ti for W in the as-grown thin films has been considered. Figure 3c shows the details of the XRD pattern obtained after the thermal treatment at 1073 K. As can be observed, the peak at 23.7° is remarkably larger than the corresponding peak in Fig. 3b. Moreover, the peak seems to be structured. For comparison, the peak positions of the WO_3 orthorhombic phase (Fig. 3d) are reported below the experimental data. As it will be discussed, both the structure of the peaks observed after annealing at 1073 K and their back-shift to higher 2θ

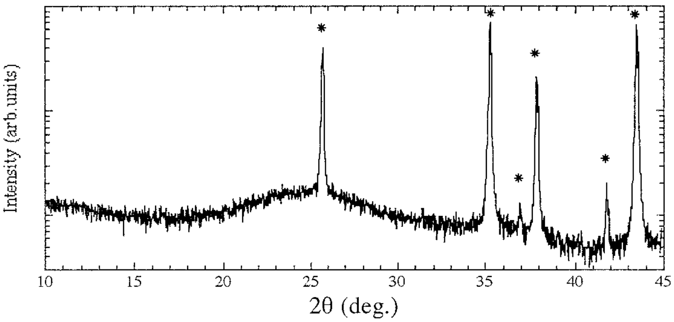

FIG. 1. X-ray diffraction pattern of the "as grown" $W_xTi_yO_z$ thin film. The intensities are in logarithmic scale. The peaks (*) present in the pattern are attributed to the Al_2O_3 substrate. The amorphous contribution can be detected in the halo ranging from 17° to 34°.

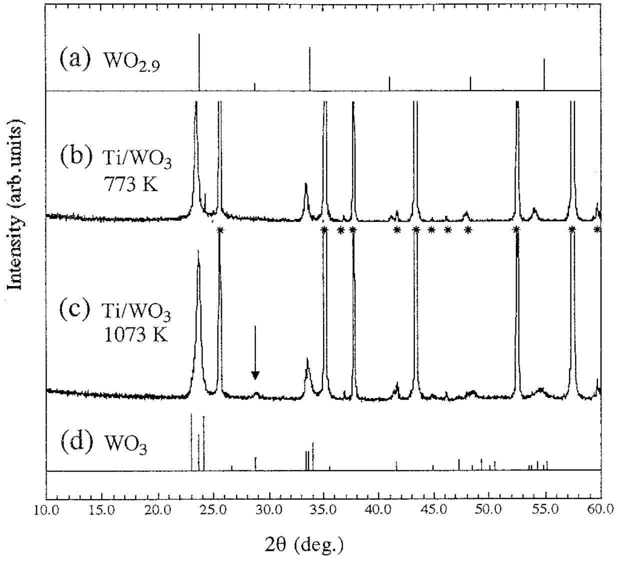

FIG. 2. X-ray diffraction patterns of the $W_xTi_yO_z$ thin film treated at 773 K (b) and of the $W_xTi_yO_z$ thin film treated at 1073 K (c). For reference, the PDF cards 18-1417 (a) and 20-1324 (d) are reported. The asterisks indicate the Al_2O_3 contribution in the XRD pattern. The arrow indicates the reflection at 28.88° appearing in the pattern at 1073 K, which is attributed to a symmetry lowering of the film structure.

TABLE 1

Calculated Lattice Spacings for $WO_{2.9}$ (Card Number in the PDF Database, 18-1417) (d_1); Experimental *d* Spacing for W–Ti–O Thin Film Measured at 773 K (d_2) and 1073 K (d_3); Cubic *d* Spacing Calculated on the Basis of a Lattice Constant a = 3.786 Å (d_4) and Corresponding *hkl* Indices

d_1 $WO_{2.9}$ (Å)	d_2, exp., 773 K (Å)	d_3, exp., 1073 K (Å)	d_4 cubic (Å)	*hkl* cubic
3.74	3.779	3.751	3.786	100
3.10		3.09		
2.65	2.676	2.670	2.677	110
2.20	2.182	2.179–2.184	2.186	111
2.02				
1.88	1.894	1.879	1.893	200
1.78				
1.67	1.695	1.679	1.693	201

angles (Fig. 3c) could be related to the titanium segregation by diffusion on the surface. Indeed, the further broadening can be caused by a transition toward the orthorhombic WO_3 phase as the peak shifts to higher 2θ angles.

The hypothesis of Ti segregation on the surface, due to annealing, has been confirmed by XPS measurements. The Ti 2*p* and W 4*f* peaks are in agreement with the literature data (18) and correspond with their higher oxidation states. The sputtered samples show for the W 4*f* signal a broadening which can be related to the presence, in addition to W(VI), of W(V). This broadening, which can be ascribed to the presence of oxygen vacancies due to the sputtering treatment, is also detected in the O 1*s* peak.

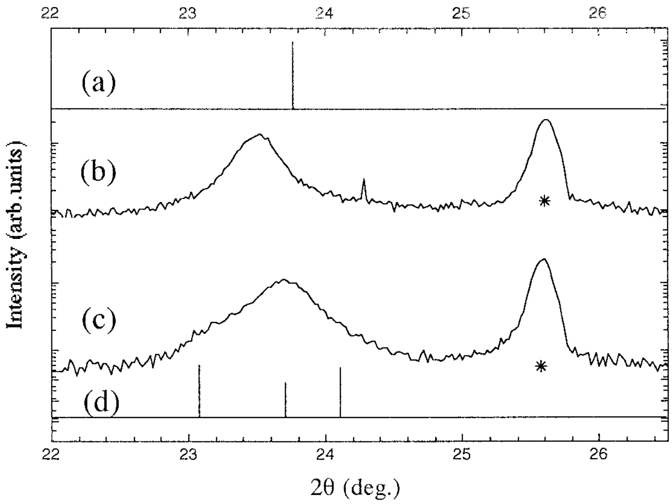

FIG. 3. Expanded view of Fig. 2 in the range 22°–26° (2θ). The logarithmic scale has been used to enhance the contribution of low intensity peaks.

TABLE 2

Ti/W Atomic Ratio Calculated on the Basis of the XPS Quantitative Analysis

Sample	Ti/W atomic ratio
As grown	0.13
Annealing at 773 K, 18 h	0.39
Annealing at 1073 K, 18 h	0.52

As shown in Table 2, the Ti/W surface atomic ratio dramatically changes from 0.39, in the case of the film treated at 773 K, to 0.52, in the case of the sample treated at 1073 K, while the as-grown sample has a surface ratio Ti/W = 0.13, which is very close to the sputtering target atomic ratio 0.11 (10/90). These results indicate that a diffusion of Ti toward the surface has been induced by the annealing treatment.

In Tables 3–5 crystallographic data of WO_3 and WO_{3-x} phases found in ICSD and PDF databases are reported. The two possible packings of $[WO_6]^{6-}$ octahedra in WO_3 phases, i.e., the cubic ReO_3-type of structure and the hexagonal one, are shown in Figs. 4a and 4b, respectively. Only one phase in the ICSD database (see Table 3) presents the hexagonal packing, while all the other structures can be described as more or less distorted cubic structures.

To the best of our knowledge, no $W_xTi_yO_z$ phase has been identified, but it is well known that *W* can enter the TiO_2 anatase structure and stabilize if (14). Moreover, in all the mixed W/Ti oxides with three or more cations, Ti and W always occupy the same sites.

The WO_3 structure is prone to host several kind of defects and, in fact, many ReO_3-related structures of WO_3 are known while only one hexagonal phase is reported in the databases. This evidence can be explained by the low formation energy for defects in the cubic structure.

Removal of oxygen in WO_3 causes the structure to collapse, introducing crystallographic shear (*CS*) planes into the crystal. A typical example of ordered *CS* planes in the structure is shown in Fig. 4c. In these structures, blocks of corner-sharing octahedra, which are typical of the ReO_3 structure, are connected by edge sharing. Similar structures are also known with three-dimensional faults, as shown in Fig. 4d. Other disorder effects in these structures can be found in (5, 19, 20, 21).

The presence of defects in the structure can cause some static disorder. The high symmetry of powder patterns obtained by introducing static disorder into the corresponding low symmetry structures is a well-known effect in molecular crystallography (22). This concept was recently applied also to ceramic structures to explain the origin of the cubic diffraction patterns of ZrO_2 nanopowders (23). In

TABLE 3
Structural Parameters and *R* Factors of the WO_3 Phases Found in the ICSD Database

	Card number	Space group	*a* (Å)	*b* (Å)	*c* (Å)	α (degrees)	β (degrees)	γ (degrees)	*R* factor (−)
WO_3	01620	*P*-1	7.309(2)	7.522(2)	7.678(2)	88.8(0)	90.9(0)	90.99	0.050
WO_3	36168	*P*-1	7.280(50)	7.480(50)	3.820(50)	90	90	90	
			7.280	7.480	7.640*				
WO_3	14332	*P*121/*n*	7.297	7.539	7.688	90	90.9	90	0.065
WO_3	15905	*P*121/*a*	7.285	7.517	3.835	90	90	90	
			7.285	7.517	7.670*				
WO_e	16080	*P*121/*n*	7.306(1)	7.540(1)	7.692(1)	90	90.9	90	0.048
WO_3	17003	*P*121/*n*	7.300	7.530	7.680	90	90.9	90	0.065
WO_3	31823	*P*121/*a*	7.274(2)	7.501(1)	3.824(3)	90	89.9	90	
			7.274	7.501	7.648*				
WO_3	00836	*Pmnb*	7.341(4)	7.570(4)	7.754(4)	90	90	90	0.061
WO_3	27961	*P*4/*nmmS*	5.272(2)	5.272(2)	3.920(2)	90	90	90	
1223°C			7.4557**	7.4557**	7.84*				
WO_3	27962	*P*4/*nmmS*	5.250(2)	5.250(2)	3.915(2)	90	90	90	
1043°C			7.425**	7.425**	7.83*				
WO_3	32001	*P*6/*mmm*	7.298(2)	7.298(2)	3.899(2)	90	90	120	0.055

To compare the cell parameters of different structures some of them have been transformed as indicated: (*) $a_{\text{transformed}} = a\sqrt{2}$, (**) $c_{\text{transformed}} = 2c$.

this case, the thermodynamically stable structure at room temperature is monoclinic, but in nanopowders it is possible to detect a cubic X-ray diffraction pattern, even if at room temperature the cubic phase is not expected.

In the case of WO_3 structures, symmetries higher than the monoclinic may result from the introduction of static disorder which can be ascribed to the presence of clusters of edge-sharing octahedra randomly distributed in the lattice. Indeed, the tendency to form edge-sharing octahedra can be found also in the oxygen-deficient WO_{3-x} phases, though in this case the edge-sharing octahedra are not randomly distributed since they are found in periodic patterns (see, e.g., Figs. 4c and 4d). In the present samples, edge sharing, which is usually found in oxygen-deficient phases, can be ascribed to the presence of titanium, which has a lower oxidation state than W, and therefore the Ti substitution for W induces the same effect of oxygen substoichiometry. This fact can justify why in the PDF database the best correspondence was found with the $WO_{2.9}$ phase. To this regard, it is interesting to note that a hypothetical mixed oxide produced from a target with a 90% W and 10% Ti composition, i.e., $W_{0.9}Ti_{0.1}O_{2.9}$, is stoichiometric with W^{+6} and Ti^{+4}.

As for disorder, in the hypothesis that Ti is randomly distributed, as is very likely since no Ti–W mixed oxide phases are known, edge sharing can also be randomly dis-

TABLE 4
Structural Parameters and *R* Factor of the Oxygen Deficient WO_{3-x} Phases Found in the ICSD Database

	Card number	Space group	*a* (Å)	*b* (Å)	*c* (Å)	α (degrees)	β (degrees)	γ (degrees)	*R* factor (−)
$W_{25}O_{73}$ ($WO_{2.92}$)	00392	*P*12/*c*1	11.93(1)	3.82(1)	59.72(1)	90	98.3(1)	90	0.088
$WO_{2.9}$	24736	*P*12/*m*1	12.100	3.780	23.400	90	95.0	90	0.088
$W_{10}O_{29}$ ($WO_{2.9}$)	27705	*P*12/*m*1	12.050	3.767	23.590	90	85.3	90	
W_5O_{14} ($WO_{2.8}$)	01509	*P*12/*m*1	23.33(1)	23.33(1)	3.797(1)	90	90	90	0.050
$W_{17}O_{47}$ ($WO_{2.76}$)	65084	*P*12/*m*1	18.840	3.787	12.330	90	102.7	90	
$W_{18}O_{49}$ ($WO_{2.72}$)	15254	*P*12/*m*1	18.334	3.786	14.044	90	115.2	90	0.065
$WO_{2.72}$	24731	*P*12/*m*1	18.320	3.790	14.040	90	115.2	90	
$W_{18}O_{49}$ ($WO_{2.72}$)	202488	*P*12/*m*1	18.318(1)	3.783(0)	14.028(2)	90	115.2	90	0.046
$W_{32}O_{84}$ ($WO_{2.625}$)	39557	*Pbam*	21.431	17.766	3.783	90	90	90	0.065

TABLE 5
Structural Parameters of the WO_3 and WO_{3-x} Phases Found in the PDF Database

	Card number	Space group	*a* (Å)	*b* (Å)	*c* (Å)	α (degrees)	β (degrees)	γ (degrees)
WO_3	20-1323	P*	7.30	7.52	7.69	88.83	90.91	90.93
WO_3	32-1395	*P*1	7.309	7.522	7.678	88.81	90.92	90.93
WO_3	43-1035	*P*21/*n*	7.297	7.539	7.688	90	90.91	90
WO_3	20-1324	—	7.384	7.512	3.846	90	90	90
WO_3	5-388	*P*4/*nmm*	5.25	5.25	3.91	90	90	90
WO_3	33-1387	*P*6/*mmm*	7.298	7.298	3.899	90	90	120
$W_{25}O_{73}$ ($WO_{2.92}$)	30-1387	*P*2/*c*	11.93	3.82	59.72	90	98.30	90
chi-$W_{20}O_{58}$ ($WO_{2.9}$)	5-386	*P*2/*m*	12.05	3.767	23.59	90	94.72	90
$WO_{2.9}$	18-1417	*P*4/*nmm*	5.30	5.30	3.83	90	90	90
$WO_{2.9}$	36-102	—	12.1	3.78	23.6	90	94.6	90
$W_{24}O_{68}$ ($WO_{2.83}$)	36-106	—	19.31	3.781	17.07	90	104.4	90
W_5O_{14} ($WO_{2.8}$)	41-745	*P*-421*m*	23.33	23.33	3.797	90	90	90
$W_{17}O_{47}$ ($WO_{2.765}$)	44-396	*P*2/*m*	18.84	3.787	12.326	90	102.67	90
$W_{18}O_{49}$ ($WO_{2.72}$)	5-392	*P*2/*m*	18.28	33.775	13.98	90	115.2	90
$W_{18}O_{49}$ ($WO_{2.72}$)	36,101	*P*2/*m*	18.324	3.784	14.035	90	115.20	90

tributed. As a consequence, the disordered defects in the WO_3 monoclinic structure, represented by edge-sharing octahedra, produce the symmetry increase observed in the XRD pattern.

Based on the data reported in the ICSD database, the XRD patterns of a selection of WO_3 phases were simulated and the results are reported in Fig. 5. These results must be compared with the simulated XRD patterns reported in Fig. 6, obtained by inducing a static disorder in the WO_3 triclinic phase (ICSD card 01620, Fig. 6a). The comparison between the ordered phases of Fig. 5 and the corresponding disordered phases of Fig. 6 shows that the structure factors are very similar. As a consequence, the description of the ordered phases displaying higher symmetry (Figs. 5b–5d) could also be reconsidered in the framework of a disordered model. In the case of Fig. 6, the disorder was simulated by increasing the cell symmetry, starting from the low-symmetry triclinic phase and keeping the fractional coordinates fixed. In this way, distributions of ions around average positions in the structure were generated and the sum of the occupancy factors of the atoms around each average position was normalized to one. In Figs. 7a and 7b the tetragonal and cubic disordered structures, generated starting from the triclinic WO_3 phase, are shown. From a structural point of view, the results of the procedure described above can be understood as a loss of correlation in the octahedral net triggered by the presence of defects (e.g., edge sharing, vacancies). Figure 7c shows how a statistic distribution of W and O ions around their "average" positions can be originated from microregions in the lattice where tilted and highly distorted octahedra are present.

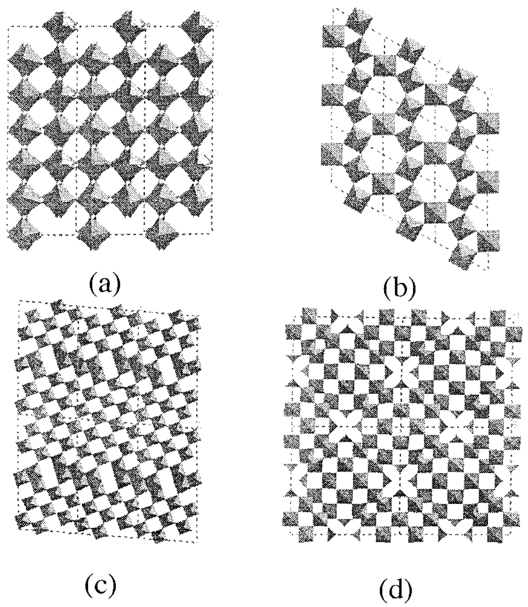

FIG. 4. Structures of (a) monoclinic WO_3 (ICSD card 14332), (b) hexagonal WO_3 (ICSD card 32001), (c) $WO_{2.9}$ (ICSD card 24736), and (d) $W_{0.7}V_{1.3}O_5$ (ICSD card 23717) phases.

Indeed, a relationship between high symmetry and disorder can be assumed considering that the high-symmetry (tetragonal) phase was identified only at high temperatures, which are expected, for thermodynamical reasons, to introduce disorder. As is well known in the case of ZrO_2, high-symmetry (e.g., cubic) phases are stabilized at low temperatures by impurities. This process has been recently discussed in terms of static disorder (23). In the case of WO_3, it was already reported that progressive inser-

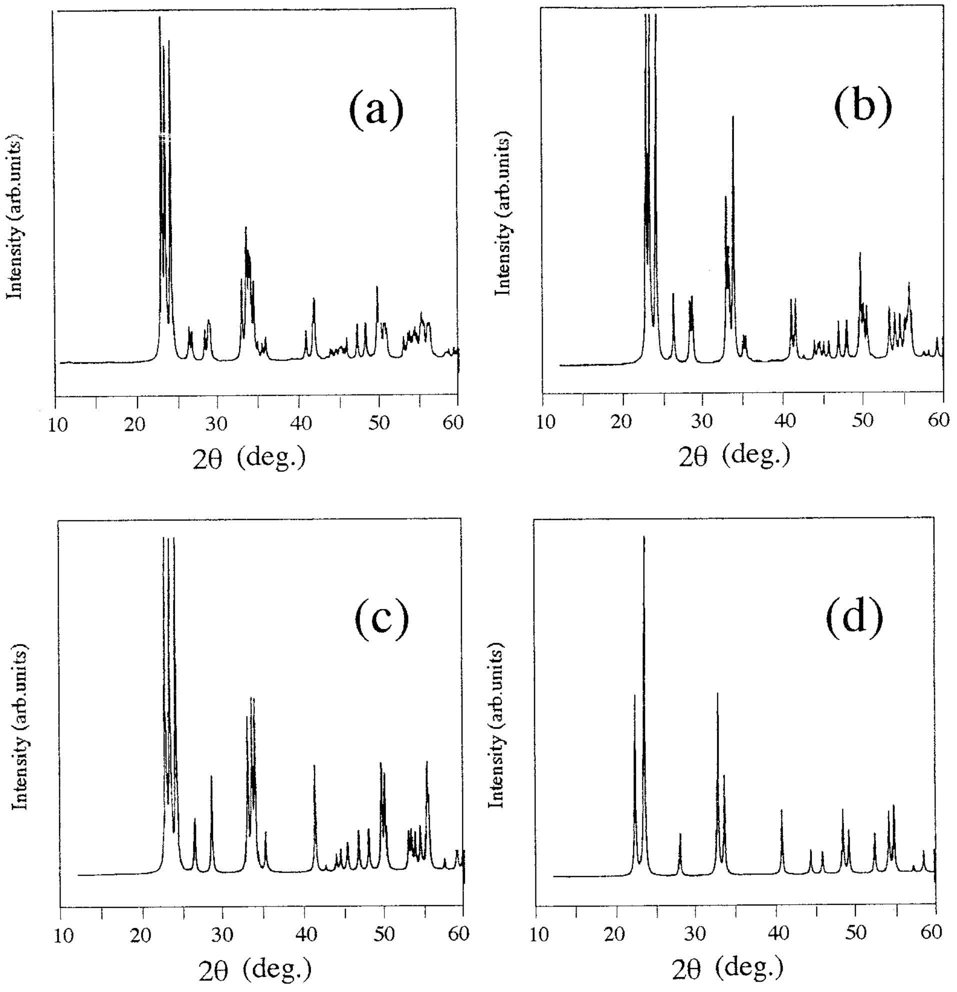

FIG. 5. Simulated XRD patterns from the ICSD database: (a) card 01620, triclinic; (b) card 14332, monoclinic; (c) card 00836, orthorhombic; (d) card 27961, tetragonal.

tion of Li in the WO_3 monoclinic structure leads to a progressive increase of the symmetry until a cubic phase appears (24). Cubic phases have also been obtained by H insertion (ICSD, card 19006). It is likely that in all these cases the high-symmetry pattern is due to structural disorder. These findings give further support to the idea that disorder effects in the Ti/WO_3 structure can be ascribed to the presence of Ti atoms.

The disordered cubic structure, which produces the simulated XRD pattern of Fig. 6e, is not present in the database. In Table 1 it is shown that the cubic phase with a cell parameter 3.786 Å well justifies the pattern obtained for the sample annealed at 773 K. The three peaks, 100, 010, and 001 reflections, in the range 23°–25° (2θ) are due to the small differences among the three axes, and the presence of only one reflection in the pattern shown in Fig. 3b can be considered as a proof of the cubic symmetry of an "average" (disordered) structure. The peak at 29.80° (2θ) in the pattern annealed at 1073 K (Fig. 2c) suggests a transformation towards an "average" tetragonal structure.

Disorder effects can also be detected through a systematic study of the structural parameters (in particular the cell volume) of the WO_3 phases found in the ICSD database. In Fig. 8 the volume of the $[WO_6]^{6-}$ structural unit of several stoichiometric WO_3 phases is plotted against the number of parameters defining the cell. This volume, $V([WO_6]^{6-})$, is defined as

$$V([WO_6]^{6-}) = V_{\text{cell}}/Z, \qquad [1]$$

where V_{cell} is the volume of the unit cell and Z is the number of ($[WO_6]^{6-}$) units in the unit cell. As can be observed, the volume of the structural unit increases with symmetry. This increase can be related to the shift toward lower 2θ angles (higher d spacing) observed for the XRD pattern of the "cubic" phase in Fig. 3b. Provided that the

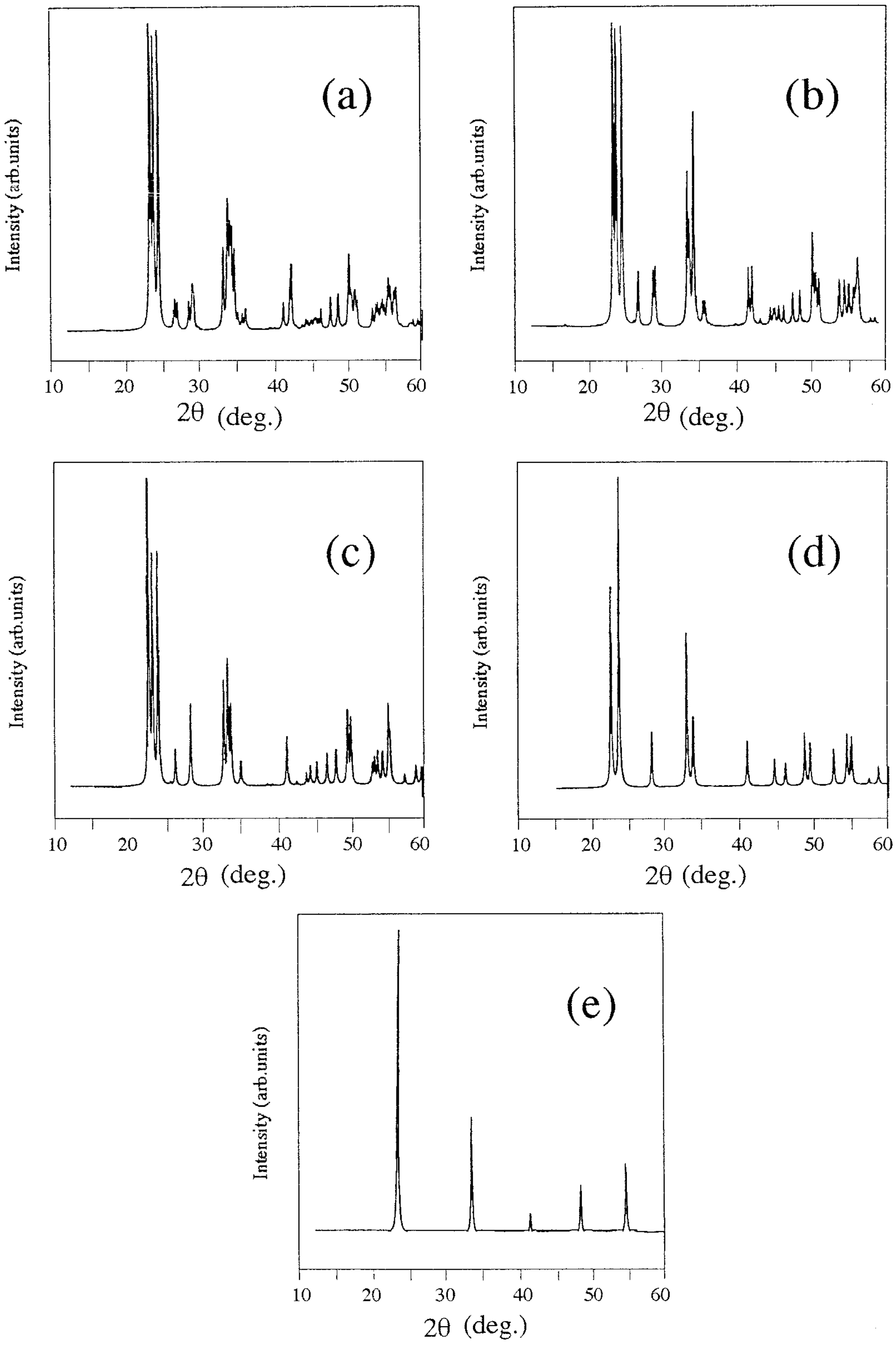

FIG. 6. Simulated XRD patterns of the phases obtained increasing the space group symmetry of the unit cell from (a) the triclinic phase (ICSD card 01620): (b) monoclinic; (c) orthorhombic; (d) tetragonal; (e) cubic.

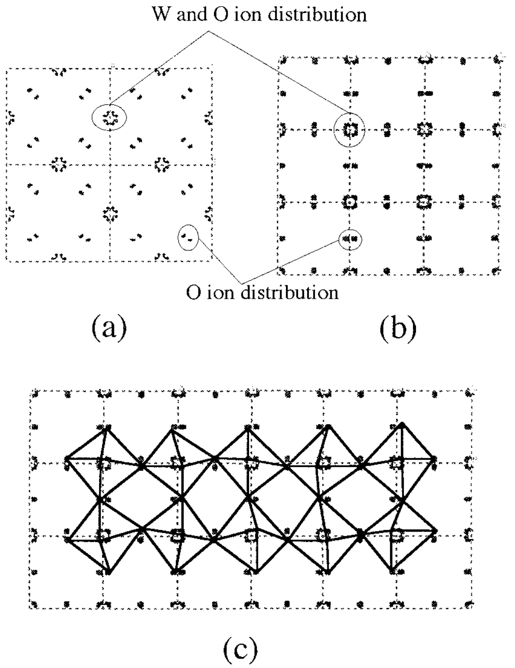

FIG. 7. Tetragonal (a) and cubic (b) disordered structures obtained by increasing the cell symmetry starting from the low-symmetry triclinic phase keeping the fractional coordinates fixed. Example of one of the possible nets of corner-sharing octahedra which originates from the distribution of ions around their average positions (c).

stoichiometry in all the considered compounds is the same, the volume increase with the symmetry of the phases may be ascribed to a disorder effect.

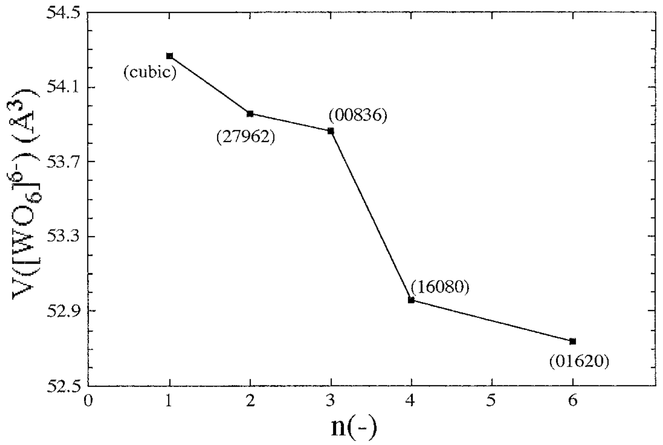

FIG. 8. Volume occupied by the $[WO_6]^{6-}$ unit in the ReO_3-type structure against the number n of parameters (triclinic, $n = 6$; monoclinic, $n = 4$; orthorhombic, $n = 3$; tetragonal, $n = 2$; cubic $n = 1$) The phases, selected from the compounds reported in Table 3 are those showing the best R factor in the cases of $n = 6$, 4, and 3; for $n = 2$ the phase at low temperature was chosen. The "cubic" phase refers to the present results.

CONCLUSIONS

The structural changes in the tungsten–titanium oxide thin films have been studied by XRD measurements and related, with the aid of XPS data, to the segregation of Ti on the film surface. Comparing our experimental results with the data available on the WO_3 phases, a disordered model for the structure has been derived. In this frame, the interplay between edge sharing and disorder has been discussed. From the analysis of the XRD data it was shown that, starting from an amorphous as-grown film, an initial ordering occurred after annealing at 773 K, but the pattern was still cubic with a cell parameter about one half that of the ordered monoclinic WO_3 phase.

After annealing at 1073 K it was possible to identify in the diffraction pattern some additional peaks which can be ascribed to a lowering of the symmetry confirmed by the structured peak at about 24° (2θ).

Even though the cause of Ti segregation is not clear, the structural changes in the film are supposed to have a close relationship with Ti concentration in the film. Structural relaxation induced by the heat treatment results in the decrease of the edge sharing defects so that cubic WO_3 phases without edge-sharing defects are formed. Ti atoms, which are known to be more stable within edge-sharing octahedra, are segregated from corner-sharing WO_6 octahedra.

Experiments for studying the kinetics of this order–disorder transformation are in progress (25), along with a study of Ti–W–O thin films surface morphology (26).

ACKNOWLEDGMENTS

We thank Marcello Zocchi for useful discussions and Sandra Boesso for technical assistance in the XPS measurements. This research has been supported by the BRITE-EURAM Project 7303 "NANOGAS". Finally, we are indebted to the editor and the reviewers of our original manuscript for their helpful suggestions and comments.

REFERENCES

1. K. Bange and T. Gambke, *Adv. Mater.* **2,** 10 (1990).
2. H. H. Kung, "Transition Metal Oxides: Surface Chemistry and Catalysis," p. 259. Elsevier, Amsterdam, 1989.
3. D. J. Smith, J. F. Vetelino, R. S. Falconer, and E. L. Wittman, *Sensors Actuators B* **13–14,** 264 (1993).
4. X. D. Wang, S. Yee, and P. Carey, *Sensors Actuators B* **13,** 458 (1993).
5. A. F. Wells, "Structural Inorganic Chemistry." Oxford Univ. Press, Oxford, 1984.
6. C. Bechinger, G. Oefinger, S. Herminghaus, P. Leiderer, *J. Appl. Phys.* **74,** 4527 (1993).
7. L. Armelao, R. Bertoncello, G. Granozzi, G. Depaoli, E. Tondello, and G. Battaglin, *J. Mater. Chem.* **4,** 407 (1994).
8. J. Tamaki, Z. Zhang, K. Fujimori, M. Akiama, T. Harada, N. Miura, and N. Yamazoe, *J. Electrochem. Soc.* **141,** 2207 (1994).
9. I. Ruokamo, T. Karkkainen, J. Huusko, T. Ruokanen, M. Blomberg, H. Torvela, and V. Lantto, *Sensors Actuators B.* **19,** 486 (1994).

10. T. Nanba, Y. Nishiyama, and I. Yasui, *J. Mater. Res.* **6,** 1324 (1991).
11. D. Davazoglou and A. Donnadieu, *J. Appl. Phys.* **72,** 1502 (1992).
12. G. Sberveglieri, L. E. Depero, S. Groppelli, and P. Nelli, *Sensors Actuators,* in press.
13. J. Gottsche, A. Hinsch, and V. Wittwer, *Solar Energy Mater. Solar Cells* **31,** 415 (1993).
14. L. E. Depero, *J. Solid State Chem.* **104,** 470 (1993).
15. J. Papp, S. Soled, K. Dwight, and A. Wold, *Chem. Mater.* **6,** 496 (1994).
16. Inorganic Crystal Structure Database (ICSD), Gmel-Institut Für Anorganische Chemie and Fachinformationszentrum FIZ Karlsruhe, 1993.
17. Powder Diffraction File, JSPDS-International Centre for Diffraction Data, Swarthmore, PA, 1994.
18. ‘‘Handbook of X-Ray Photoelectron Spectroscopy’’ (G. E. Mullerberg, Ed.), Perkin–Elmer Corporation.
19. R. J. D. Tilley, ‘‘Deffect Crystal Chemistry.’’ Blackie, New York, 1987.
20. B. G. Hyde and S. Andersson, ‘‘Inorganic Crystal Structures.’’ Wiley, New York, 1989.
21. K. Kosuge, Chemistry of Non-stoichiometric Compounds.’’ Oxford Science, New York, 1994.
22. A. I. Kitaigorodsky, ‘‘Molecular Crystals and Molecules.’’ Academic Press, New York, 1973.
23. L. E. Depero and P. Levrangi, *J. Solid State Chem.* **110,** 190 (1994).
24. K. H. Cheng and M. S. Whittingham, *Solid State Ionics* **1,** 151 (1980).
25. L. E. Depero, I. Natali-Sora, C. Perego, L. Sangaletti, and G. Sberveglieri, *Sensors Actuators B,* in press.
26. G. Sberveglieri, L. E. Depero, P. Nelli, S. Groppelli, F. Ronconi, and L. Sangaletti, submitted.